

Numerical models of the thermomechanical evolution of planetesimals: Application to the acapulcoite-lodranite parent body

Gregor J. GOLABEK^{1,2*}, Bernard BOURDON², and Taras V. GERYA¹

¹ETH Zurich, Institute of Geophysics, Sonneggstrasse 5, 8092 Zurich, Switzerland

²Laboratoire de Géologie de Lyon, ENS Lyon, CNRS and Université Claude Bernard de Lyon, 46 Allée d'Italie, 69364 Lyon Cedex 07, France

*Corresponding author. E-mail: gregor.golabek@erdw.ethz.ch

(Received 07 September 2013; revision accepted 16 March 2014)

Abstract—The acapulcoite-lodranite meteorites are members of the primitive achondrite class. The observation of partial melting and resulting partial removal of Fe-FeS indicates that this meteorite group could be an important link between achondrite and iron meteorites, on the one hand, and chondrite meteorites, on the other. Thus, a better understanding of the thermomechanical evolution of the parent body of this meteorite group can help improve our understanding of the evolution of early planetesimals. Here, we use 2-D and 3-D finite-difference numerical models to determine the formation time, initial radius of the parent body of the acapulcoite-lodranite meteorites, and their formation depth inside the body by applying available geochronological, thermal, and textural constraints to our numerical data. Our results indicate that the best fit to the data can be obtained for a parent body with 25–65 km radius, which formed around 1.3 Ma after calcium-aluminum-rich inclusions. The 2-D and 3-D results considering various initial temperatures and the effect of porosity indicate possible formation depths of the acapulcoite-lodranite meteorites of 9–19 and 14–25 km, respectively. Our data also suggest that other meteorite classes could form at different depths inside the same parent body, supporting recently proposed models (Elkins-Tanton et al. 2011; Weiss and Elkins-Tanton 2013).

INTRODUCTION

Geochemical data and astronomical observations indicate that planetesimals, the building blocks of terrestrial planets and sources of meteorites, have formed within the first few million years after the formation of the first solids in the solar system (e.g., Kleine et al. 2009). Several numerical models have focused on the thermal evolution of these objects (e.g., Ghosh and McSween 1998; Merk et al. 2002; Hevey and Sanders 2006; Sahijpal et al. 2007; Henke et al. 2012). However, most of these studies were based on 1-D models assuming that conduction is the main mechanism cooling the interior of these objects. There is ample evidence suggesting that conductive cooling is not the only mechanism involved. First, increasing evidence for early magnetic fields in meteorite parent bodies argues for efficient cooling of the initially hot planetesimals (Weiss et al. 2008; Fu et al. 2012;

Tarduno et al. 2012), which requires more efficient heat transport than conduction through solid material. Second, the accretion time scale of these bodies in the first few million years after the beginning of the solar system suggests that heat produced by decay of ²⁶Al was sometimes sufficient to melt them, which indicates that liquid-state convection could have played a role. Third, work by Tkalcec et al. (2013) shows that meteorite parent bodies could have experienced solid-state deformation, which cannot be explained by melt extraction processes or impact processes and cannot be studied using 1-D models.

Recently, an increasing number of workers argued that planetesimals with up to several hundred kilometer radii formed rapidly via the gravitational or streaming instability mechanism, thus many of the meteorite parent bodies could be such primordial asteroids, which experienced only a very short accretion history (Johansen et al. 2007; Cuzzi et al. 2008, 2010;

Morbidelli et al. 2009; Chambers 2010; Johansen and Klahr 2011; Parisi 2013) of tens to hundreds of years.

Here, we studied the thermal and deformation history of already accreted planetesimals. As 2-D models have a smaller surface-to-volume ratio compared with 3-D, this can result in an artificially slower cooling of the interior. To estimate the importance of this effect, we performed in this study both 2-D and 3-D thermomechanical models considering both conduction and advection processes. We have also compared numerical 2-D and 3-D results with analytical 1-D radial heat conduction models (Carslaw and Jaeger 1959) to estimate under which conditions pure solid-state conduction models can be safely applied.

It has been argued that small planetesimals might have initially a high porosity (Cuzzi et al. 2008). However, it has also been suggested that cold isostatic pressing reduces the porosity of planetesimals with radii ranging from 20 to 50 km largely and that for even larger objects, the initial porosity is already low throughout almost all of the body (Henke et al. 2012). To test the possible effect of an initially high porosity, we performed also 2-D models considering this effect.

Additionally, we have put constraints on the formation time and radius of the acapulcoite-lodranite parent body for which geochronological data on the thermal history are available. These were then compared with previous constraints on radius and formation time, relying on analytical thermal evolution models and radiometric data (e.g., Touboul et al. 2009).

The structure of the manuscript is the following: In the next section, we describe the constraints on the thermal evolution of planetesimals with a focus on the acapulcoite-lodranite parent body. This is followed by a discussion of the numerical model and model setup. The last two sections contain our findings and the discussion.

CONSTRAINTS ON THE THERMAL HISTORY OF PLANETESIMALS

In this section, we summarize various sets of observations derived from petrology, major and trace element geochemistry, and isotope geochemistry on the thermal history of the parent bodies of meteorites. There are several types of observations, which can be used to constrain the thermal history of planetesimals. First, the accretion time scale provides a first-order indication on the potential amount of heating due to ^{26}Al decay. In this respect, one should clearly distinguish between the time scale of accretion and the time scale of core formation. As shown in Qin et al. (2008), there should be an offset between the two time

scales because the temperature increase due to the conversion of gravitational energy is insufficient for heating bodies <1000 km significantly. Notably, for small bodies, the minimum temperature for melting a Fe-FeS alloy will not be reached, preventing an efficient iron-silicate separation (Schubert et al. 1986). Thus, the core formation will take place at the pace of ^{26}Al decay, i.e., it should take on the order of several ^{26}Al half-lives to reach the peak temperature inside the body. Second, the degree of melting at a given pressure reached in basaltic achondrites can provide an estimate of mantle temperatures. This can be done either by considering the major element chemistry, especially if petrological experiments for the required bulk compositions are available or by using the trace element contents to derive rough estimates of the degree of melting (see below). Third, in some cases, it is possible to derive cooling rates for planetesimals. As the closure temperature for some isotope systems has been determined experimentally (e.g., Van Orman et al. 2006), it is possible to use this information to derive cooling rates. In addition, it is possible to use siderophile elements in achondrites (e.g., Righter and Drake 1996) to derive the temperatures of metal-silicate equilibration during core formation; this should possibly represent the maximum temperatures reached in a planetesimal. In numerous cases, the thermal history of planetesimals such as the acapulcoite-lodranite parent body can be perturbed by impacts (Rubin 2007). The effect of impacts can be to disrupt planetesimals entirely, in which case, the cooling rates can increase by orders of magnitude (e.g., Benedix et al. 2010). Alternatively, a recent study has shown that impacts can significantly increase the cooling rate by modifying the shape of planetesimals (Davison et al. 2013). In what follows, we summarize the information obtained so far using these various methods for the acapulcoite-lodranite parent body.

Time Scale of Accretion and Metal segregation in the Acapulcoite-Lodranite Parent Body

Based on an Hf-W study of acapulcoites and lodranites combined with thermal modeling of their parent body, it was concluded that the acapulcoite-lodranite parent body accreted between 1.5 and 2 Ma after calcium-aluminum-rich inclusions (CAI) (Touboul et al. 2009). Such an early age of accretion indicates that the main source of heating was due to heating by ^{26}Al rather than by impacts as, for small objects, impact heating is insufficient to cause extensive heating (e.g., Keil et al. 1993). It should be noted also that silicate melting reaches 20% for the case of lodranites, which indicates again that impact heating could not be the

sole source of heating. One should note, however, that this age is derived from a combination of Hf-W dating with simplified solid-state conduction models for the acapulcoite-lodranite parent body (A-LPB) and should therefore be considered as a first-order approximation. If the A-LPB had accreted much earlier than 1 Ma after CAI, then most likely it would have experienced significant melting, which is not observed. Indeed, the Hf/W ratios of acapulcoites and lodranites are similar to that of ordinary chondrites, which indicates that any episode of metal segregation must have been limited and kept the Hf/W ratio close to its original chondritic value. The Hf-W ages of acapulcoites and lodranites based on internal isochrons yield ages of 5 to almost 6 Ma after CAI, and these represent the oldest radiometric ages measured for this class of meteorites. This is consistent with the idea that the closure temperature of Hf-W is the highest (975–1025 °C) compared with other chronometers. This relatively late accretion is thus consistent with the observation that no significant metal segregation did take place as heating due to ^{26}Al decay was insufficient.

Conditions and Timing of Mantle Melting

The geochemical and petrological observations of acapulcoites and lodranites provide important information about the melting conditions and allow a classification of these meteorites according to their thermal evolution. There is a clear distinction between the acapulcoites showing almost no indication of silicate melting, while the most evolved lodranites experienced up to 20% silicate melting (McCoy et al. 1996, 1997; Floss 2000). The most primitive acapulcoites have not experienced any melt separation, while the more evolved ones have lost some Fe-FeS alloy. This corresponds to a minimum eutectic temperature of approximately 980 °C for the Fe-FeS alloy for pressures ranging between 0 and 3 GPa (Usselman 1975). A higher temperature could also have been reached, corresponding to lower S contents in the metallic alloy. More evolved acapulcoites would have reached higher temperatures, but their maximum temperatures should not have exceeded the silicate solidus (around 1120 °C for a peridotite composition at low pressure; Hirschmann 2000). As mentioned before, evolved lodranites were heated to higher temperatures and have lost up to 20% silicate as shown by the REE patterns depleted in light rare earths. One can estimate that the corresponding temperature is approximately 100 °C above the solidus, assuming isobaric peridotite melting at low pressure (Herzberg et al. 2000; Hirschmann 2000; Trønnes and Frost 2002; Wade and Wood 2005).

Thermal History of the Acapulcoite-Lodranite Parent Body

The interpretation of the late-stage cooling of the acapulcoite-lodranite parent body for temperatures ranging between 800 and 120 °C is rather complex. First thermometry based on mineralogy indicates rather fast cooling rates (Zipfel et al. 1995) in contrast to cooling rates using fission track dating or K/Ar. Thus, it has been suggested that the fast cooling recorded by mineralogical indicators was due to disruption of the parent body by an impact, while the later history could be explained by re-accretion to explain the slow cooling rate near 120 °C (Göpel and Manhès 2010). It is thus relevant as in Göpel and Manhès (2010) to consider several stages of cooling including slowing cooling until 4555 Ma followed by a rapid cooling due to a disruptive impact as witnessed in the mineralogy of acapulcoites (Rubin 2007). This late-stage shock-heating event has probably also reset isotope systems such as Ar-Ar and U-Th-He, both with low closure temperatures, and has been called upon to explain veins of metal and sulfides, metallic copper, or ovoid regions of opaque blebs inside orthopyroxenes (McCoy et al. 1996). One possible interpretation of these observations is that the A-LPB cooled from its peak temperature until 4555 Ma where it reached the closure temperature of U-Pb in apatite (350–650 °C) as reported in Göpel and Manhès (2010). This time would represent the timing of impact and the mineralogical textures associated with this impact described in Rubin (2007) would date from this time. It is worth noting also that this impact event at 4555 Ma did not entirely reset the whole rock U-Pb system as the latter records an age of 4562 Ma, which is possibly slightly younger than the oldest Hf-W age (Touboul et al. 2009). If we estimate the closure temperature of silicates to 700–800 °C, then this would give an additional anchor for the cooling curve of the acapulcoites.

A subsequent reassembly would then explain the slow late-stage cooling. One should note in addition that some acapulcoites show up to 6% relict chondrule grains that indicate that they were not submitted to long-term heating at temperatures where extensive recrystallization of silicates takes place. In this respect, these samples (e.g., GRA98028) may be analogs of Portales Valley, a so-called H7 chondrite that has reached peak temperatures similar to acapulcoites (Ruzicka et al. 2005). Note that these samples were not analyzed in the study of Touboul et al. (2009); thus, it is possible that their thermal record and associated chronology was different.

Table 1 presents a summary of the temperatures and timing of accretion for the acapulcoite-lodranite

Table 1. Comparison of the acapulcoite-lodranite group with other known achondrite meteorite groups.

Meteorite group	t_{acc} [Ma]	t_{core} [Ma]	T_{peak} [°C]	T_{magm} [°C]	T_{core} [°C]
Eucrites	0–4 (1)	1–4 (1,2)	1530 (3,4)	1150–1190 (5,6)	1530 (3,4)
Angrites	<2 (7)	<2 (7)	$>T_{\text{liquidus}}$ (8)	1180 (9)	1900 (10)
Acapulcoites-lodranites	1.5–2 (11)	N/A	1000–1200 (11)	1200 (11)	N/A

t_{acc} = accretion time; t_{core} = core formation time; T_{peak} = peak temperature; T_{magm} = magmatic temperature; T_{core} = core formation temperature.

References: (1) Touboul et al. (2008), (2) Kleine et al. (2009), (3) Righter and Drake (1996), (4) Righter and Drake (1997), (5) Stolper (1975), (6) Stolper (1977), (7) Kleine et al. (2012), (8) Longhi (1999), (9) Jurewicz et al. (1993), (10) Righter (2008), (11) Touboul et al. (2009).

parent body, together with a comparison with two other achondrite families, namely eucrites and angrites, which could be compiled from literature data. These observations are used to constrain the thermal model described in the next section.

Constraints on Initial Temperature of the Protoplanetary Disk

The temperature at the midplane of the protoplanetary disk, which sets the initial starting temperature of the planetesimal T_{space} , is in reality a time-dependent parameter. Depending on the amount of viscous heating due to stellar mass accretion, the disk temperature can vary in the first approximately 10^6 yr in the inner part of the disk over more than one order of magnitude (Davis 2005; Min et al. 2011). Thus, a significantly different initial temperature—and during later evolution surface temperature—can potentially affect the results for early-formed planetesimals. In the case of the A-LPB, Zipfel et al. (1995) have shown that the abundance of moderately volatile elements with a 50% condensation temperature of 600 K in this body was depleted by a factor of two relative to CI chondrites. This could indicate that if the A-LPB formed at a time when the nebula was still present that the disk temperature reached up to 600 K, but this clearly represents only an upper limit. It could well be that the nebula gas had been removed by the time of accretion and that the disk temperature was already lower.

NUMERICAL MODEL

To study the thermal evolution of early-formed planetesimals and constrain the original size and formation time of the acapulcoite-lodranite parent body, we consider here both two- and three-dimensional creeping flow using the extended Boussinesq approximation, which can account for both thermal and chemical buoyancy forces applying the finite-difference code family I2ELVIS/I3ELVIS (Gerya and Yuen 2007). For this purpose, we solve the equations of mass,

momentum, and energy conservation. Additionally, we compute the location-dependent gravity field by solving the Poisson equation. We assume a temperature-, pressure-, strain rate-, and melt fraction-dependent silicate rheology (Pinkerton and Stevenson 1992; Ranalli 1995). Relevant code features not given in the publication mentioned above are described here.

Batch-Melting Model for Silicates

A batch-melting model assuming a peridotite composition is included. Parameterizations for both the solidus and liquidus temperatures, T_{sol} and T_{liq} of peridotite are applied (Herzberg et al. 2000; Wade and Wood 2005). For $T \leq T_{\text{sol}}$, the silicate melt fraction ϕ is zero, for $T \geq T_{\text{liq}}$, it is equal to 1. In the intermediate temperature range $T_{\text{sol}} < T < T_{\text{liq}}$, the melt fraction is assumed to increase linearly with temperature according to the following relation (Burg and Gerya 2005):

$$\phi = \frac{T - T_{\text{sol}}}{T_{\text{liq}} - T_{\text{sol}}}. \quad (1)$$

Both consumption and release of latent heat due to melting and freezing of silicates are taken into account.

Consequently, the effective density ρ_{eff} of partially molten rocks varies with the fraction of silicate melt ϕ , additionally to its dependence on temperature T , pressure P , and composition c (see Gerya and Yuen 2007). The effective density is assumed to vary linearly with the melt fraction (Burg and Gerya 2005):

$$\rho_{\text{eff}}(c, P, T, \phi) = \rho_{\text{Si-sol}}(c, P, T) - \phi [\rho_{\text{Si-sol}}(c, P, T) - \rho_{\text{Si-liq}}(c, P, T)] \quad (2)$$

where $\rho_{\text{Si-sol}}$ and $\rho_{\text{Si-liq}}$ are the densities of the solid and liquid silicates, respectively.

The presence of a silicate melt fraction $\phi > 0.1$ also has an influence on the effective viscosity of the silicate material η_{eff} , which is described as follows (Pinkerton and Stevenson 1992):

$$\eta_{\text{eff}} = \eta_{\text{Si-liq}} \exp \left\{ \left[2.5 + \left(\frac{1-\phi}{\phi} \right)^{0.48} \right] (1-\phi) \right\} \quad (3)$$

Within a narrow silicate melt fraction range, the silicate behavior undergoes a transition from a solid-like material to a low-viscosity crystal suspension (see Solomatov 2007; Costa et al. 2009). Thus, the viscosity of largely molten silicates $\eta_{\text{Si-liq}}$ is approximately 10^{-4} to 10^2 Pa s (Rubie et al. 2003; Liebske et al. 2005). Hence, due to the low viscosity, both the Rayleigh Ra and the Nusselt number Nu will be high and cooling will be a very efficient process.

Effective Thermal Conductivity of Largely Molten Silicates

Due to numerical restrictions, the lower cut-off viscosity in the numerical model is $\eta_{\text{num}} = 10^{17}$ Pa s, orders of magnitude higher than realistic viscosities for largely molten silicates. Taking the dependency of the effective viscosity of partially molten silicates on temperature T , strain-rate $\dot{\epsilon}$, and melt fraction ϕ (see Gerya and Yuen 2007) into account, one can calculate (see Equation 3) that the effective viscosity of partially molten silicate material in the numerical model is always close to the cut-off viscosity value η_{num} . It was suggested that the heat flux from a magma ocean (Solomatov 2007) can be described using the so-called soft turbulence model (Kraichnan 1962; Siggia 1994). In this model, the expected convective heat flux q is given as:

$$q = 0.089 \frac{k(T - T_{\text{surf}})}{L} Ra^{1/3} \quad (4)$$

where the Rayleigh number Ra is defined as

$$Ra = \frac{\alpha g (T - T_{\text{surf}}) \rho_{\text{eff}}^2 c_P D^3}{k \eta_{\text{Si-liq}}} \quad (5)$$

α , is the thermal expansivity, g is the gravitational acceleration, T is the potential temperature, T_{surf} is the surface temperature, k is the thermal conductivity, and D is the depth of the magma ocean.

Depending on the actual silicate melt viscosity in the numerical model η_{num} , one can estimate an increased effective thermal conductivity k_{eff} by using the theoretically expected heat flux from a magma ocean q from Equation 4. This effective thermal conductivity can simulate the heat flux of a medium with a realistic magma ocean viscosity (Zahnle et al. 1988; Tackley et al. 2001; Hevey and Sanders 2006;

Golabek et al. 2011), despite our numerical limitations. Combining Equations 4 and 5, this can be done using the following expression for the effective thermal conductivity k_{eff} :

$$k_{\text{eff}} = \left(\frac{q}{0.089} \right)^{3/2} \frac{1}{(T - T_{\text{surf}})^2 \rho_{\text{eff}}} \left(\frac{\alpha g c_P}{\eta_{\text{num}}} \right)^{-1/2} \quad (6)$$

Porosity Treatment

The effect of cold isostatic pressing due to self-gravity of a planetesimal on the porosity ϕ is considered as described in recent literature (Henke et al. 2012):

$$\phi(p) = 0.42 + 0.46 \left[\left(\frac{p}{p_0} \right)^{1.72} + 1 \right]^{-1} \quad (7)$$

where p is the internal pressure and p_0 is a constant.

Also, the influence of porosity on both the bulk density of solid silicates and its thermal conductivity is taken into account as described elsewhere (Henke et al. 2012).

The density of solid silicates is considered to vary linearly with the porosity:

$$\rho_{\text{Si-por}}(c, P, T, \phi) = \rho_{\text{Si-sol}}(c, P, T)(1 - \phi) \quad (8)$$

For $\phi < 0.2$, the thermal conductivity of the solid silicates is given by:

$$k_1(\phi) = k e^{-\phi/\phi_0} \quad (9)$$

where ϕ_0 is a constant.

In case $\phi > 0.4$, the following equation is used:

$$k_2(\phi) = k e^{a-\phi/\phi_1} \quad (10)$$

where a and ϕ_1 are constants.

Finally, for the intermediate case $0.2 \leq \phi \leq 0.4$, we use the following equation:

$$k_3(\phi) = [k_1^4(\phi) + k_2^4(\phi)]^{1/4} \quad (11)$$

For $T > 700$ K (Yomogida and Matsui 1984) we consider that the sintering process further reduces the porosity of the solid silicate material. For this purpose, we use the model described elsewhere in more detail (Yomogida and Matsui 1984; Henke et al. 2012).

Based on Henke et al. (2012), the change of the porosity due to sintering can be given as:

$$\frac{\partial\phi}{\partial t} = A(1 - \phi) \frac{\sigma^{3/2}}{\mathfrak{R}^3} \exp\left(-\frac{E'_a}{RT}\right) \quad (12)$$

A is a constant value, σ is the effective stress on the contact faces of two grains, \mathfrak{R} is the effective grain size, E'_a is the apparent activation energy of the sintering process, and R is the universal gas constant, respectively.

For the constants in Equations 7, 9, 10, and 12, we adopt here the values as suggested elsewhere (Schwenn and Goetze 1978; Henke et al. 2012).

Model Setup

The numerical model boxes in 2-D and 3-D Cartesian geometry have dimensions of 500×500 km and $(520)^3$ km, respectively. The meteorite parent body ($R_p = 25\text{--}105$ km) is surrounded by the so-called sticky air layer (e.g., Schmeling et al. 2008), which has an almost zero density, a constant temperature, and a constant viscosity ($\eta_{SA} = 10^{17}$ Pa s). It has been shown that this approach allows simulating both a free surface (Cramer et al. 2012) and an infinite reservoir to absorb heat released from the planetary body (Golabek et al. 2011; Tkalcec et al. 2013). The grid employed in 2-D has 501×501 grid points, while generally, $(261)^3$ grid points are employed in 3-D. Correspondingly, the standard numerical grid resolution is 1 km in 2-D and 2 km in 3-D, respectively. Additionally, we performed resolution tests in 3-D geometry with $(101)^3$ and $(501)^3$ grid points, corresponding to 5.2 and 1.04 km grid resolution, respectively.

As the potential energy released upon accretion of the planetesimals considered here results only in a small temperature increase (Schubert et al. 1986), we neglect this effect and assume an isothermal initial temperature field. As a reference value, we use $T_{space} = T_{SA} = 290$ K (Ghosh and McSween 1998). To test the effect of the uncertain temperature at the midplane, we perform additional calculations with two different initial temperatures, namely 170 and 400 K (see also Tables 2 and 3). For the sake of simplicity, the spherical planetesimal is assumed to be completely composed of silicates. For this purpose, an olivine rheology is applied (Ranalli 1995). This is reasonable as olivine is the most abundant mineral in typical mantle composition and is weaker relative to pyroxenes, thus controlling deformation (Mackwell 1991).

To test the effect of the initial porosity of the planetesimal on the thermomechanical evolution, we perform several calculations assuming an initial porosity

of $\phi_{init} = 0.5$ throughout the corresponding planetesimal (Henke et al. 2012) and model the change of porosity as described in the Porosity Treatment section.

For all models, we consider time-dependent radioactive heating by both short- (^{26}Al) and long-lived (^{40}K , ^{235}U , ^{238}U , ^{232}Th) radiogenic isotopes. In the early solar system, ^{26}Al is by far the dominant radioactive energy source and the initial $^{26}\text{Al}/^{27}\text{Al}$ is taken as 5.85×10^{-5} (Thrane et al. 2006), this value representing an upper limit for the abundance of ^{26}Al (see Jacobsen et al. 2008). All other physical parameters are reported in Table 2.

In the model runs, we vary both the radius R_p and the instantaneous formation time t_{form} of the planetesimals. While radii between 25 and 105 km are considered, the instantaneous formation time is varied in fractions of the half-life time of ^{26}Al , namely between 0 and 2.92 Ma after CAI formation, thus reducing the amount of available radiogenic (especially ^{26}Al) heating (see also Table 3).

RESULTS

General Results

The comparison between peak temperatures predicted by the analytical solid-state conduction model (Carslaw and Jaeger 1959) and both 2-D and 3-D numerical results shows that for models assuming a late formation where radiogenic heating by ^{26}Al is weak, the analytical and the numerical models agree very well. For higher temperatures, the results start to deviate due to onset of convective heat transport and temperature buffering caused by latent heat effects, which are both not considered in the analytical model (see Fig. 1). This allows the numerical models to avoid extremely high internal temperatures comparable to the vaporization temperature of forsterite as suggested by the analytical model. As expected, the cooling in 2-D is less efficient than in 3-D calculations, resulting in slightly higher peak temperatures in 2-D models compared with 3-D results. As mentioned above, differences between 2-D and 3-D calculations are mainly related to a different surface-to-volume ratio in cylindrical and spherical planetary geometries, respectively. A resolution test in 3-D shows good convergence; thus, a resolution of $(261)^3$ grid points appears to be sufficient for the 3-D calculations (see Fig. 1).

Application to the Acapulcoite-Lodranite Parent Body

The following constraints are used to estimate whether the temperature evolution at a certain depth d matches the characteristics of the A-LPB in order to

Table 2. Physical parameters.

Parameter	Symbol	Value	Units	Reference
Parent body radius	R_P	25–105	km	
Instantaneous formation time	t_{form}	0–2.92	Ma	
Density of uncompressed silicate melt	$\rho_{\text{Si-liq}}$	2900	kg m^{-3}	(1,2)
Density of uncompressed solid silicates	$\rho_{\text{Si-sol}}$	3500	kg m^{-3}	(1)
Temperature of space (sticky air)	T_{space}	170–400	K	(3,4)
Activation energy	E_a	470	kJ mol^{-1}	(5)
Dislocation creep onset stress	σ_0	3×10^7	Pa	(6)
Power law exponent	n	4		(5)
Latent heat of silicate melting	L_{Si}	400	kJ mol^{-1}	(3,6)
Silicate melt fraction at rheological transition	ϕ_{crit}	0.4		(7,8)
Heat capacity of silicates	c_P	1000	$\text{J (kg}\cdot\text{K)}^{-1}$	(6)
Thermal expansivity of solid silicates	$\alpha_{\text{Si-sol}}$	3×10^{-5}	1/K	(2)
Thermal expansivity of molten silicates	$\alpha_{\text{Si-liq}}$	6×10^{-5}	1/K	(2)
Thermal conductivity of solid silicates	k	3	$\text{W (m}\cdot\text{K)}^{-1}$	(9)
Thermal conductivity of molten silicates	k_{eff}	$\leq 10^6$	$\text{W (m}\cdot\text{K)}^{-1}$	
Minimum thermal conductivity of unsintered solid silicates	k_{low}	10^{-3}	$\text{W (m}\cdot\text{K)}^{-1}$	(10,11)
Temperature at onset of hot sintering	T_{sint}	700	K	(10)
Initial porosity before cold isostatic pressing	ϕ_{init}	0.5		(11)

References: (1) Stolper et al. (1981), (2) Suzuki et al. (1998), (3) Ghosh and McSween (1998), (4) Barshay and Lewis (1976), (5) Ranalli (1995), (6) Turcotte and Schubert (2002), (7) Solomatov (2007), (8) Costa et al. (2009), (9) Tarduno et al. (2012), (10) Yomogida and Matsui (1984), (11) Henke et al. (2012).

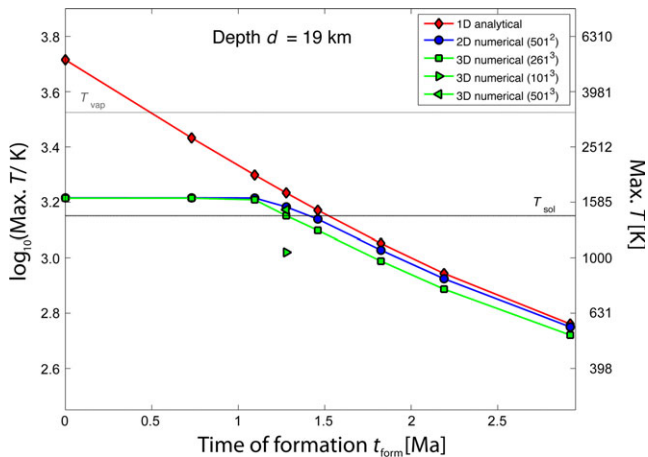


Fig. 1. Comparison between peak temperatures predicted for different formation times t_{form} by the analytical solid-state conduction model (red diamonds), 2-D model results (blue circles), and 3-D model results (green squares) for a depth of 19 km inside a body with 45 km radius. 3-D resolution test data are shown by a green right-pointing triangle (101^3 grid points) and a green left-pointing triangle (501^3 grid points). For comparison, the solidus temperature of peridotite (Herzberg et al. 2000) and the vaporization temperature of forsterite (Benz et al. 1989) at low pressures are shown as black and gray lines, respectively. (see online version for color figure.)

find a body from which both types of meteorites could be derived:

1. Possible acapulcoite temperature evolutions must match geochronological data within error bars and peak temperatures must exceed the Fe-FeS eutectic

temperature, but stay below the peridotite solidus at all times.

2. Possible lodranite temperature evolutions must match geochronological data within error bars and the peak temperatures must exceed the peridotite solidus by at least 50 K, but stay at all times within 100 K of the peridotite solidus temperature.
3. Cooling curves for candidate depths must be undisturbed, as this indicates active solid-state deformation, which is inconsistent with the texture of acapulcoite-lodranites.

Reference Case: $T_{\text{space}} = 290 \text{ K}$

Analysis of the 2-D results shows that for all studied radii, objects with formation times $t_{\text{form}} \leq 1.095 \text{ Ma}$ may fit the geochronological data for certain depths; however, it is not possible to find fits that also match the thermal constraints for acapulcoites and lodranites (see circles in Fig. 2). Additionally, possible fits exhibit strong perturbations of the cooling curves, indicating that solid-state deformation (see Fig. 3b for 3-D example) in the form of cooler downwellings and resultant warm upwellings occurred (Elkins-Tanton et al. 2008; Tkalcic et al. 2013).

On the other hand, for all studied radii, objects that formed at $t_{\text{form}} \geq 1.825 \text{ Ma}$ show even in their deep interior insufficient internal temperatures to match the peak temperatures observed in the A-LPB, thus excluding any possible matches (see circles in Fig. 2).

A special case are the models with $R_P = 25 \text{ km}$, where models starting at 1.095 Ma and earlier display

Table 3. List of numerical models.

Model	Radius R_P [km]	Formation time t_{form} [Ma]	Geometry	Grid points	T_{space} [K]	Initial porosity?
alp01	25	0	2-D	501 × 501	290	No
alp02	25	0.73	2-D	501 × 501	290	No
alp03	25	1.095	2-D	501 × 501	290	No
alp04	25	1.2775	2-D	501 × 501	290	No
alp05	25	1.46	2-D	501 × 501	290	No
alp06	25	2.19	2-D	501 × 501	290	No
alp07	25	2.92	2-D	501 × 501	290	No
alp08	35	0	2-D	501 × 501	290	No
alp09	35	0.73	2-D	501 × 501	290	No
alp10	35	1.095	2-D	501 × 501	290	No
alp11	35	1.2775	2-D	501 × 501	290	No
alp12	35	1.46	2-D	501 × 501	290	No
alp13	35	1.825	2-D	501 × 501	290	No
alp14	35	2.19	2-D	501 × 501	290	No
alp15	35	2.92	2-D	501 × 501	290	No
alp16	45	0	2-D	501 × 501	290	No
alp17	45	0.73	2-D	501 × 501	290	No
alp18	45	1.095	2-D	501 × 501	290	No
alp19	45	1.2775	2-D	501 × 501	290	No
alp20	45	1.46	2-D	501 × 501	290	No
alp21	45	1.825	2-D	501 × 501	290	No
alp22	45	2.19	2-D	501 × 501	290	No
alp23	45	2.92	2-D	501 × 501	290	No
alp24	65	0	2-D	501 × 501	290	No
alp25	65	0.73	2-D	501 × 501	290	No
alp26	65	1.095	2-D	501 × 501	290	No
alp27	65	1.2775	2-D	501 × 501	290	No
alp28	65	1.46	2-D	501 × 501	290	No
alp29	65	1.825	2-D	501 × 501	290	No
alp30	65	2.19	2-D	501 × 501	290	No
alp31	65	2.92	2-D	501 × 501	290	No
alp32	75	0	2-D	501 × 501	290	No
alp33	75	0.73	2-D	501 × 501	290	No
alp34	75	1.095	2-D	501 × 501	290	No
alp35	75	1.2775	2-D	501 × 501	290	No
alp36	75	1.46	2-D	501 × 501	290	No
alp37	75	2.19	2-D	501 × 501	290	No
alp38	75	2.92	2-D	501 × 501	290	No
alp39	85	0	2-D	501 × 501	290	No
alp40	85	0.73	2-D	501 × 501	290	No
alp41	85	1.095	2-D	501 × 501	290	No
alp42	85	1.2775	2-D	501 × 501	290	No
alp43	85	1.46	2-D	501 × 501	290	No
alp44	85	1.825	2-D	501 × 501	290	No
alp45	85	2.19	2-D	501 × 501	290	No
alp46	85	2.92	2-D	501 × 501	290	No
alp47	95	1.46	2-D	501 × 501	290	No
alp48	95	1.825	2-D	501 × 501	290	No
alp49	105	0	2-D	501 × 501	290	No
alp50	105	0.73	2-D	501 × 501	290	No
alp51	105	1.095	2-D	501 × 501	290	No
alp52	105	1.2775	2-D	501 × 501	290	No
alp53	105	1.46	2-D	501 × 501	290	No
alp54	105	2.19	2-D	501 × 501	290	No

Table 3. *Continued.* List of numerical models.

Model	Radius R_p [km]	Formation time t_{form} [Ma]	Geometry	Grid points	T_{space} [K]	Initial porosity?
alp55	105	2.92	2-D	501 × 501	290	No
alp56	45	0	3-D	261 × 261 × 261	290	No
alp57	45	0.73	3-D	261 × 261 × 261	290	No
alp58	45	1.095	3-D	261 × 261 × 261	290	No
alp59	45	1.2775	3-D	261 × 261 × 261	290	No
alp60	45	1.2775	3-D	101 × 101 × 101	290	No
alp61	45	1.2775	3-D	501 × 501 × 501	290	No
alp62	45	1.46	3-D	261 × 261 × 261	290	No
alp63	45	1.825	3-D	261 × 261 × 261	290	No
alp64	45	2.19	3-D	261 × 261 × 261	290	No
alp65	45	2.92	3-D	261 × 261 × 261	290	No
alp66	25	1.095	2-D	501 × 501	170	No
alp67	25	1.2775	2-D	501 × 501	170	No
alp68	25	1.46	2-D	501 × 501	170	No
alp69	35	1.095	2-D	501 × 501	170	No
alp70	35	1.2775	2-D	501 × 501	170	No
alp71	35	1.46	2-D	501 × 501	170	No
alp72	45	1.095	2-D	501 × 501	170	No
alp73	45	1.2775	2-D	501 × 501	170	No
alp74	45	1.46	2-D	501 × 501	170	No
alp75	65	1.095	2-D	501 × 501	170	No
alp76	65	1.2775	2-D	501 × 501	170	No
alp77	65	1.46	2-D	501 × 501	170	No
alp78	75	1.095	2-D	501 × 501	170	No
alp79	75	1.2775	2-D	501 × 501	170	No
alp80	75	1.46	2-D	501 × 501	170	No
alp81	25	1.095	2-D	501 × 501	400	No
alp82	25	1.2775	2-D	501 × 501	400	No
alp83	25	1.46	2-D	501 × 501	400	No
alp84	35	1.095	2-D	501 × 501	400	No
alp85	35	1.2775	2-D	501 × 501	400	No
alp86	35	1.46	2-D	501 × 501	400	No
alp87	35	1.825	2-D	501 × 501	400	No
alp88	45	1.095	2-D	501 × 501	400	No
alp89	45	1.2775	2-D	501 × 501	400	No
alp90	45	1.46	2-D	501 × 501	400	No
alp91	45	1.825	2-D	501 × 501	400	No
alp92	65	1.095	2-D	501 × 501	400	No
alp93	65	1.2775	2-D	501 × 501	400	No
alp94	65	1.46	2-D	501 × 501	400	No
alp95	65	1.825	2-D	501 × 501	400	No
alp96	75	1.095	2-D	501 × 501	400	No
alp97	75	1.2775	2-D	501 × 501	400	No
alp98	75	1.46	2-D	501 × 501	400	No
alp99	75	1.825	2-D	501 × 501	400	No
alp100	25	1.095	2-D	501 × 501	290	Yes
alp101	25	1.2775	2-D	501 × 501	290	Yes
alp102	25	1.46	2-D	501 × 501	290	Yes
alp103	35	1.095	2-D	501 × 501	290	Yes
alp104	35	1.2775	2-D	501 × 501	290	Yes
alp105	35	1.46	2-D	501 × 501	290	Yes
alp106	45	1.095	2-D	501 × 501	290	Yes
alp107	45	1.2775	2-D	501 × 501	290	Yes
alp108	45	1.46	2-D	501 × 501	290	Yes

Table 3. *Continued.* List of numerical models.

Model	Radius R_P [km]	Formation time t_{form} [Ma]	Geometry	Grid points	T_{space} [K]	Initial porosity?
alp109	65	1.095	2-D	501 × 501	290	Yes
alp110	65	1.2775	2-D	501 × 501	290	Yes
alp111	65	1.46	2-D	501 × 501	290	Yes
alp112	75	1.095	2-D	501 × 501	290	Yes
alp113	75	1.2775	2-D	501 × 501	290	Yes
alp114	75	1.46	2-D	501 × 501	290	Yes

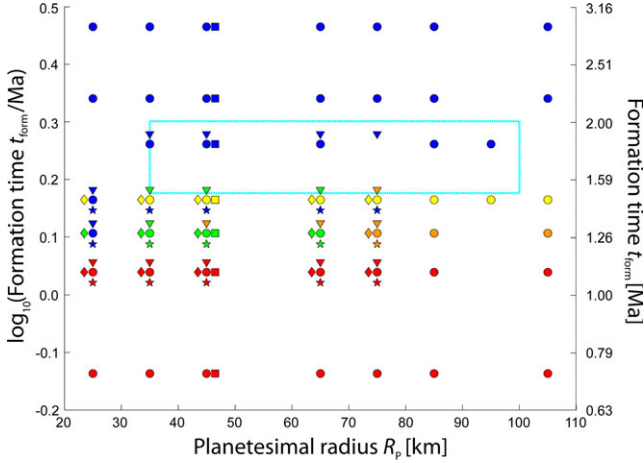


Fig. 2. Results of models varying formation time t_{form} and planetesimal radius R_P . Red: Peak temperature for possible geochronological data match above thermal constraints, occurrence of solid-state deformation and/or no fit with all geochemical data possible. Blue: Peak temperature for possible geochronological data match below Fe-FeS eutectic melting and/or no fit with all geochemical data possible. Yellow: Match with all geochronological data; however, insufficient peak temperature for lodranites. Orange: Match with geochronological data possible; however, solid-state deformation observed. Green: Match with both geochronological data and thermal constraints, no solid-state deformation observed. Circles represent 2-D results for the reference case with $T_{\text{space}} = 290$ K, while five-pointed stars and downward-pointing triangles stand for models with $T_{\text{space}} = 170$ and 400 K, respectively. Diamonds depict 2-D models considering an initial porosity and squares stand for 3-D results. 2-D data points for models with smaller and higher T_{space} are shifted on the y -axis for clarity reasons, while for the same purpose, 2-D models considering an initial porosity and 3-D data points are slightly shifted on the x -axis. The cyan box indicates the radius and formation time range suggested by Touboul et al. (2009) based on pure solid-state conduction models. (see online version for color figure.)

too high peak temperatures, while models starting at 1.2775 Ma and later experience peak temperatures too low to give a reasonable match (see circles in Fig. 2).

For $R_P \geq 35$ km and $t_{\text{form}} = 1.46$ Ma, the geochronological data and thermal constraints for acapulcoites can be matched at depths of 15–18 km; however, possible fits to the lodranite geochronological data exhibit insufficient temperatures to match the observed peak temperature (see circles in Fig. 2).

Thermal, geochronological, and deformational constraints can all be fulfilled in the 2-D models best by planetesimals with $R_P = 35$ –65 km and instantaneous accretion times ranging from $1.095 < t_{\text{form}} < 1.46$ Ma after CAI formation (see Fig. 2). Best fits are obtained for depth of 11–14 km for acapulcoites and 16–19 km for lodranites, respectively (see Fig. 4a).

To test these 2-D results, we performed a set of additional 3-D calculations for $R_P = 45$ km (see Table 3), which exhibit generally similar results with peak temperatures exceeding the constraints and solid-state deformation at depths allowing us to fit geochronological data for $t_{\text{form}} \leq 1.095$ Ma (see square symbols in Figs. 2 and 3), while bodies formed at $t_{\text{form}} \geq 1.825$ Ma are too cold in their interiors. Best matches—without displaying downwellings at the relevant depths—can be obtained for $t_{\text{form}} = 1.2775$ and 1.46 Ma. However, for the latter case, possible fits to the lodranite geochronological data do not reach peak temperatures in the observed range (see Fig. 2). Compared with the 2-D results, the 3-D models suggest deeper layers at 19 and 22–23 km for the origin of the acapulcoites and lodranites, respectively (see Fig. 4b). This difference in depth fit is related to the surface-to-volume ratio discussed above. As the general behavior agrees among the 2-D and 3-D models, it seems likely that the 2-D results can provide a good estimate for the size and accretion time of the A-LPB.

Cases with Different Initial Temperature: $T_{\text{space}} = 170$ K and 400 K

Varying the initial temperature changes the time frame in which good fits with both geochronological and temperature constraints can be obtained. On the other hand, it has only minor influence on the radius range in which relevant bodies can be found. In detail, reducing the initial temperature to 170 K does not change the radius-formation time range with fitting models as these models have sufficient short-lived radiogenic elements to still reach sufficiently high temperatures to match the constraints. However, for later-formed objects, the initially lower temperature leads to results that are not able to match at least part of the constraints (see five-pointed stars in Fig. 2).

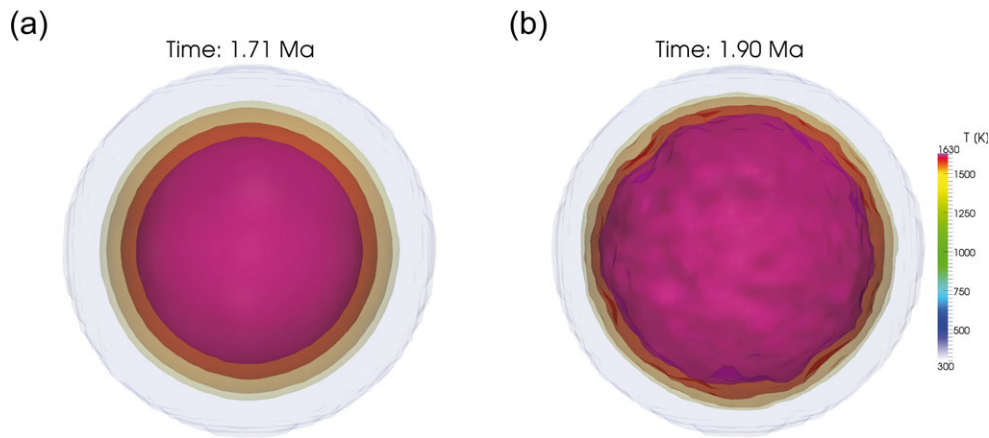


Fig. 3. Examples of 3-D thermal structure of planetesimal with $R_P = 45$ km and $t_{\text{form}} = 0.73$ Ma after CAI at (a) 0.98 Ma and (b) 1.17 Ma after model start. The bluish contour marks the surface of the planetesimal, while the colored contours show the 1400 K (yellow), 1500 K (orange), 1600 K (red), and 1630 K (purple) isotherms, respectively. Due to the onset of short-lived Rayleigh-Taylor instabilities, the thermal structure in (b) deviates with time significantly from the initial classical onion shell structure as seen in (a). See also Video S1. (see online version for color figure.)

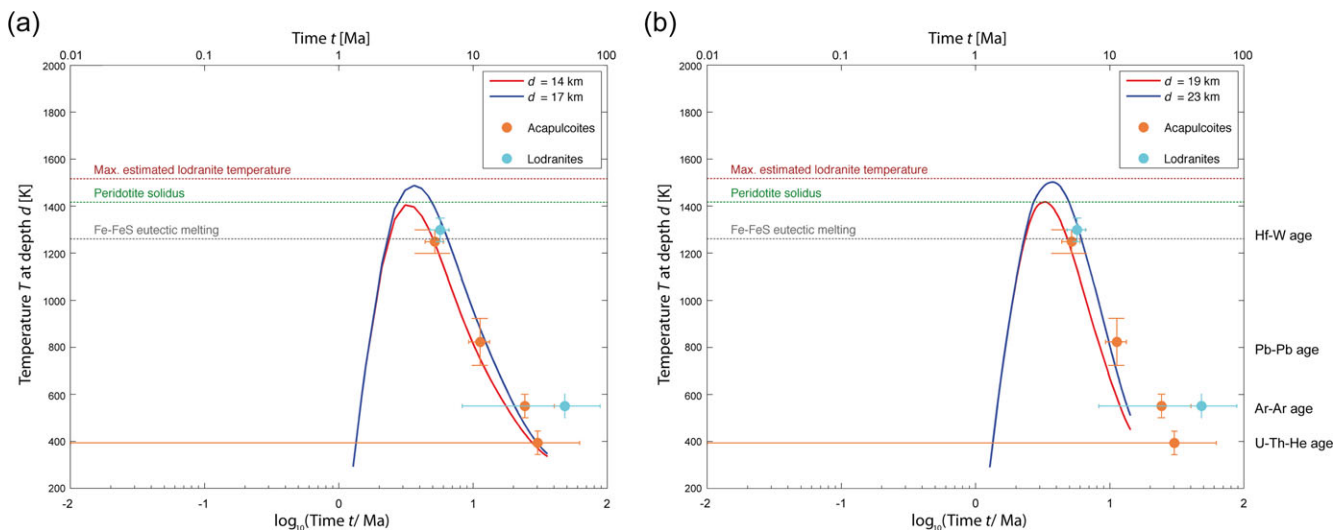


Fig. 4. Best-fit thermal evolution for planetesimal with $R_P = 45$ km and $t_{\text{form}} = 1.2775$ Ma based on (a) 2-D model alp19 and (b) 3-D model alp59 (see also Table 3). Geochronological data are based on Touboul et al. (2009) and references therein.

Matches with acapulcoites can be made at depths of 14–18 km, while best fits with the constraints for lodranites are obtained for depths of 20–25 km, thus shifting the depths to larger values compared with the 2-D reference case applying a higher initial temperature.

On the other hand, an increase in the initial temperature to 400 K extends the time frame in which fitting models can be found to later formation times up to 1.46 Ma after CAI formation. Due to the longer presence of a hot, low viscosity interior downwellings can form inside larger planetesimals, which form around 1.27 Ma after CAI, narrowing the radius range of fits. For a formation time of 1.46 Ma after CAI

formation conditions are comparable to those in the reference model as fits can be obtained for radii ranging from 35 to 65 km (see downward-pointing triangles in Fig. 2). Thermal evolutions fitting the constraints for acapulcoites and lodranites can be found at depths of 12–17 km and 19–21 km, respectively.

Cases with Initial Porosity

In models with initial porosity, the sintering temperature is quickly reached at larger depths inside the planetesimals; thus the thermal conductivity increases quickly, theoretically allowing for more efficient heat transport from the deeper interior.

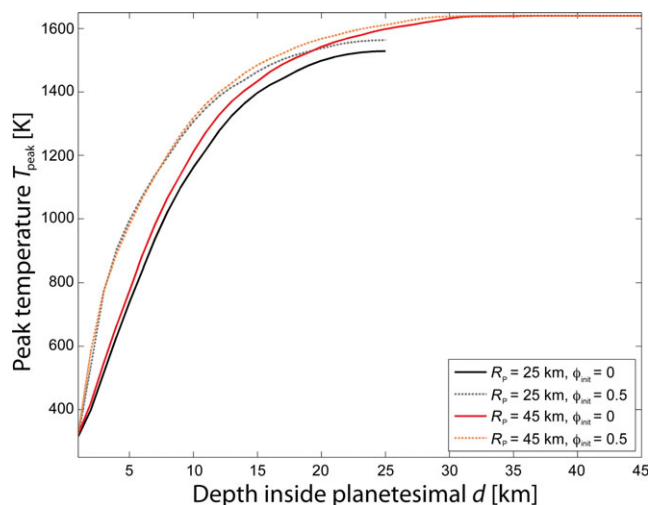


Fig. 5. Comparison of peak temperatures reached inside planetesimals with $R_p = 25$ and $R_p = 45$ km and $t_{\text{form}} = 1.2775$ Ma after CAI without taking porosity into account (solid lines in black and red) and with initial porosity (dash-dotted lines in gray and orange). (see online version for color figure.)

However, these models also tend to retain a porous several kilometer thick surface layer and thus low thermal conductivity as these layers never become warm enough for efficient sintering processes to occur. Due to the presence of this low conductivity layer hindering the heat transport, higher temperatures can be reached at the same depth compared with models neglecting porosity effects (see Fig. 5). Compared with the models without initial porosity, the temperature evolutions matching all constraints are generally found at more shallow depths around 9–12 km for acapulcoites and for 14–17 km for lodranites, respectively. Within the frame of tested formation times, porosity does not allow for later formation times of the A-LPB compared with models without porosity. As described by Henke et al. (2012), porosity is most effective on small bodies, for example, the isolating properties of the porous layers allow also smaller bodies with $R_p = 25$ km and $t_{\text{form}} = 1.2775$ Ma to experience in very limited depth regions temperature evolutions in agreement with all constraints (see Figs. 2 and 5).

DISCUSSION

Our models suggest that the acapulcoite-lodranite parent body had an initial radius in the range between 25 and 65 km. Within this range, geochronological, thermal, and textural constraints for both meteorite groups can be fitted with both 2-D and 3-D numerical models. This range in radius is in good agreement with the values suggested for the initial radius of planetesimals formed via gravitational instability

discussed above and overlaps with the radii suggested previously (35–100 km, Touboul et al. 2009). However, our models indicate that an earlier formation of the A-LPB than suggested previously (1.5–2 Ma after CAI formation)—based on analytical solid-state conduction models—is possible (see Fig. 2). While no effect of initial porosity on viable formation times could be found, its insulating effect allows for smaller parent bodies and shallower formation depth of both acapulcoites and lodranites.

The occurrence of solid-state deformation inside the larger planetesimals studied here can be explained using a simplified model. For time scales shorter than the characteristic diffusion time, the mechanism inducing solid-state deformation can be treated as a Rayleigh-Taylor instability (Conrad and Molnar 1997). The time needed to develop a Rayleigh-Taylor instability t_{instab} depends both on the viscosity and on the thickness of the unstable layer. On the basis of both 2-D and 3-D results, we obtain the transient thickness of the part of the thermal boundary layer whose viscosity ranges between $10^{17} < \eta < 10^{24}$ Pa s, which will be called d_{BL}' . This gives an upper limit for the thickness of the more deformable part of the thermal boundary layer. Thus, on the basis of numerical results, we obtain for the stages of cooling relevant for acapulcoites and lodranites a typical thickness d_{BL}' on the order of 10 km. Using the simplification of assuming a constant viscosity for the entire layer, we can obtain an estimation of the minimum instability time t_{instab} , which is defined here as the time in which the amplitude of the instability increases by a factor of 100. The instability time is compared with the time scale during which the interior of the corresponding planetesimal cools sufficiently to prevent solid-state deformation at the depths relevant for the formation of lodranites. Here, we estimate this by obtaining the time when the lodranite formation region cools sufficiently to reach a viscosity of 10^{24} Pa s, preventing any significant solid-state deformation. Figure 6 shows analytical growth rates for Rayleigh-Taylor instabilities for the simplified case of plane geometry (Conrad and Molnar 1997) for different viscosities η_{top} for the overlying, denser layer assuming the continuous presence of a low viscosity layer of 10^{17} Pa s below.

On small bodies, only instabilities with very small viscosities can grow on a shorter time scale than the characteristic diffusion time given by $t_{\text{char}} = d_{\text{BL}}^2 \rho c_p / k$, (for values see Table 2) on which the density variations caused by temperature differences, will be smoothed out. However, due to the small viscosity contrast, necking can occur and the resulting downwellings are unstable and short-lived (see also Video S1). On small bodies, the cooling is too fast to allow for any

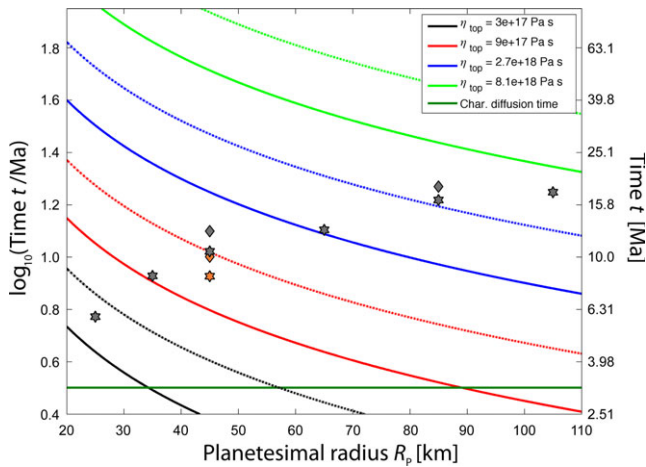


Fig. 6. Instability time scales of dominant wavelength of Rayleigh-Taylor instabilities for respective viscosity η_{top} of overlying, dense lid material (colored lines) for different thicknesses of this unstable layer (dash-dotted lines for $d_{\text{BL}}' = 6$ km and solid lines for $d_{\text{BL}}' = 10$ km) compared with the growth time of the thermal boundary to the depth relevant to the formation of lodranites based on 2-D (grayish) and 3-D results (orange). Six-pointed stars stand for models with $t_{\text{form}} = 0.73$ Ma, while diamond symbols represent models with $t_{\text{form}} = 1.2775$ Ma after CAI formation. For details on the models represented by the different symbols, see also Table 3. Only instabilities growing faster than the characteristic diffusion time (here for $d_{\text{BL}}' = 10$ km) can grow (solid olive line), while the slower growing ones are smoothed out. (see online version for color figure.)

significant growth of Rayleigh-Taylor instabilities with larger viscosity contrasts (see Fig. 6). On the other hand, Rayleigh-Taylor instability times are smaller on larger bodies due to their larger gravity acceleration and the cooling of the interior of these bodies takes longer (see Fig. 6). During the more extended cooling time, a thicker thermal boundary layer (Sotin and Labrosse 1999) can form, allowing for the growth of instabilities with larger viscosity contrasts on time scales shorter than the characteristic diffusion time scale (see Fig. 6 and Video S2). Due to their higher viscosity, these downwellings are less prone to necking and thus longer lived and can induce textural changes in larger bodies (see Fig. 2) as observed in certain meteorites (Tkalcic et al. 2013).

One has to keep in mind that in reality, the viscosity structure of the planetesimals will be evolving over time. Thus, large early-formed planetesimals experiencing a stronger radiogenic heating will contain a low-viscosity interior for a longer time, while small bodies formed late might never be able to form an internal low-viscosity layer, resulting in negligible growth rates for Rayleigh-Taylor instabilities. Thus, small bodies can avoid altogether any solid-state

deformation during their early evolution. Thus, the theoretical calculations presented here should only be regarded as a first-order approximation of observed processes.

Both 2-D and 3-D results indicate that the surface layers of the A-LPB are cool enough to avoid Fe-FeS eutectic melting, thus possibly retaining their original chondritic composition. In contrast, their deep interiors experienced temperatures significantly above the peridotite solidus, thus even for large dihedral angles as observed in static experiments for both the olivine-Fe-FeS system (Ballhaus and Ellis 1996; Minarik et al. 1996) and the peridotite-Fe-FeS system (Bagdassarov et al. 2009), efficient iron-silicate separation could occur in their deep interiors via the rainfall mechanism (Stevenson 1990; Rubie et al. 2003, 2007; Höink et al. 2006). These observations are in agreement with previous work suggesting chondritic surface layers overlying differentiated interiors (Elkins-Tanton et al. 2011; Weiss and Elkins-Tanton 2013).

Finally, it should be mentioned that our results also indicate that pure solid-state conduction models can only be applied safely for late-formed planetesimals, requiring more sophisticated numerical models to study the evolution of early-formed planetary objects such as Vesta (Hans et al. 2013), the angrite parent body (Kleine et al. 2012), or iron meteorites (e.g., Markowski et al. 2006). In this respect, this model cannot be considered to be generic. In those bodies, more extensive heating results in massive differentiation that is not considered in the model presented here.

Model Limitations

In the present study, we assume spherically shaped planetesimals, while it has been suggested that planetesimals with radii considered here experience several hundred collisions during their early evolution (Davison et al. 2013). This can result in an irregular shape of the final body and due to the larger surface area of such an irregular body in a faster cooling of its interior. While the current models suggest only small effects related to porosity, its typical initial value is uncertain and a larger range of possible initial porosities should be tested in the future.

Due to the weak gravity and the small internal pressures in the discussed planetary bodies, one expects small Darcy velocities for melt migration; however, the possible intrusion of melt into overlying layers could influence the thermal evolution and thus should be tested in the future with numerical models considering two-phase flow equations. Related to that, ^{26}Al partitioning into the melt can result in a faster cooling of the interior (Sahijpal et al. 2007) and this effect was

not considered here. If one considers that the degree of partial melting reached a maximum of 20% while the partition coefficient of Al is 0.2, this implies that 55% of Al would be retained in the residue during melting, assuming 100% extraction of the partial melt. In typical successful models, silicate melting would only occur between 2.5 and 5 Ma after accretion with the peak being reached around 4 Ma (see Fig. 4). As this is late compared with the short half-life time of ^{26}Al , the residual heat produced by ^{26}Al partitioned at the peak of melting into the crust would represent a maximum of 0.9% of the initial heat production. Thus, although this effect would ultimately need to be taken into account, it probably would not drastically change the outcome of our models.

One should also mention that we ignored the presence of iron in the planetary body. The effect of potential energy release due to iron-silicate separation is very small on the small bodies considered here (Schubert et al. 1986), e.g., assuming a chondritic body with 10 vol% iron and 65 km radius, the mean temperature increase due to core formation would be <1 K. However, the effect of latent heat buffering when chondritic material reaches the Fe-FeS eutectic melting might reduce peak internal temperatures. Thus, this effect should also be investigated in the future using a two-phase flow model as mentioned before. Clearly, these aspects require further work to test their effect on the results presented here.

CONCLUSIONS

The results suggest that 2-D and 3-D numerical models, although computationally more expensive than 1-D models, can help obtain a more realistic thermomechanical evolution of planetesimal interiors. As these models are able to capture solid-state deformation processes, this allows us to apply additional textural constraints on the formation time and original radius of the acapulcoite-lodranite parent body, which helps to narrow down the possible initial radius considerably. Our results indicate that the lodranites and acapulcoites were probably formed at a depth of approximately 10–25 km within a body with a radius of 25–65 km and the corresponding temperature evolution is consistent with the observational evidence we have for these meteorites. This approach can also be applied to other meteorite parent bodies to improve our understanding of their early evolution.

Acknowledgments—We thank the reviewers A. Rubin, T. Davison, and T. McCoy for constructive comments, which helped to improve the manuscript. GJG thanks N. Coltice, S. Labrosse, and F. Nimmo for helpful

discussions. GJG was supported by SNF grant PBEZP2-134461.

Editorial Handling—Dr. Nancy Chabot

REFERENCES

- Bagdassarov N., Golabek G. J., Solferino G., and Schmidt M. W. 2009. Constraints on the Fe-S melt connectivity in mantle silicates from electrical impedance measurements. *Physics of the Earth and Planetary Interiors* 177:139–146.
- Ballhaus C. and Ellis D. J. 1996. Mobility of core melts during Earth's accretion. *Earth and Planetary Science Letters* 143:137–145.
- Barshay S. S. and Lewis J. S. 1976. Chemistry of primitive solar material. *Annual Review of Astronomy and Astrophysics* 14:81–94.
- Benedix G. K., McCoy T. J., Keil K., and Love S. G. 2010. A petrologic study of the IAB iron meteorites: Constraints on the formation of the IAB-Winonaite parent body. *Meteoritics & Planetary Science* 35:1127–1141.
- Benz W., Cameron A. W. G., and Melosh H. J. 1989. The origin of the Moon and the single impact hypothesis III. *Icarus* 81:113–131.
- Burg J.-P. and Gerya T. V. 2005. The role of viscous heating in Barrovian metamorphism of collisional orogens: Thermomechanical models and application to the Lepontine Dome in the Central Alps. *Journal of Metamorphic Geology* 23:75–95.
- Carslaw H. S. and Jaeger J. C. 1959. *Conduction of heat in solids*, 2nd ed. Oxford: Oxford University Press. 510 p.
- Chambers J. E. 2010. Planetesimal formation by turbulent concentration. *Icarus* 208:505–517.
- Conrad C. P. and Molnar P. 1997. The growth of Rayleigh-Taylor-type instabilities in the lithosphere for various rheological and density structures. *Geophysical Journal International* 129:95–112.
- Costa A., Caricchi L., and Bagdassarov N. 2009. A model for the rheology of particle-bearing suspensions and partially molten rocks. *Geochemistry Geophysics Geosystems* 10: Q03010.
- Cramer F., Schmeling H., Golabek G. J., Duret T., Orendt R., Buitter S. J. H., May D. A., Kaus B. J. P., Gerya T. V., and Tackley P. J. 2012. A comparison of numerical surface topography calculations in geodynamic modelling: An evaluation of the “sticky air” method. *Geophysical Journal International* 189:38–54.
- Cuzzi J. N., Hogan R. C., and Shariff K. 2008. Toward planetesimals: Dense chondrule clumps in the protoplanetary nebula. *The Astrophysical Journal* 687:1432–1447.
- Cuzzi J. N., Hogan R. C., and Bottke W. F. 2010. Towards initial mass functions for asteroids and Kuiper Belt objects. *Icarus* 208:518–538.
- Davis S. S. 2005. Condensation front migration in a protoplanetary nebula. *The Astrophysical Journal* 620:994–1001.
- Davison T. M., O'Brien D. P., Ciesla F. J., and Collins G. S. 2013. The early impact histories of meteorite parent bodies. *Meteoritics & Planetary Science* 48:1894–1918.
- Elkins-Tanton L. T., Maroon E., Krawczynski M. J., and Grove T. L. 2008. Magma ocean solidification processes

- on Vesta (abstract #1364). 39th Lunar and Planetary Science Conference. CD-ROM.
- Elkins-Tanton L. T., Weiss B. P., and Zuber M. T. 2011. Chondrites as samples of differentiated planetesimals. *Earth and Planetary Science Letters* 305:1–10.
- Floss C. 2000. Complexities on the acapulcoite-lodranite parent body: Evidence from trace element distributions in silicate minerals. *Meteoritics & Planetary Science* 35:1073–1085.
- Fu R. R., Weiss B. P., Shuster D. L., Gattacceca J., Grove T. L., Suavet C., Lima E. A., Li L., and Kuan A. T. 2012. An ancient core dynamo in asteroid Vesta. *Science* 338:238–241.
- Gerya T. V. and Yuen D. A. 2007. Robust characteristics method for modelling multiphase visco-elasto-plastic thermo-mechanical problems. *Physics of the Earth and Planetary Interiors* 163:83–105.
- Ghosh A. and McSween H. Y. 1998. A thermal model for the differentiation of asteroid 4 Vesta, based on radiogenic heating. *Icarus* 134:187–206.
- Golabek G. J., Keller T., Gerya T. V., Zhu G., Tackley P. J., and Connolly J. A. D. 2011. Origin of the Martian dichotomy and Tharsis from a giant impact causing massive magmatism. *Icarus* 215:346–357.
- Göpel C. and Manhès G. 2010. The thermal history of the Acapulco meteorite and its parent body deduced from U/Pb systematics in mineral separates and bulk rock fragments. *Comptes Rendus Geoscience* 342:53–59.
- Hans U., Kleine T., and Bourdon B. 2013. Rb-Sr chronology of volatile depletion in differentiated protoplanets: BABI, ADOR and ALL revisited. *Earth and Planetary Science Letters* 374:204–214.
- Henke S., Gail H.-P., Trieloff M., Schwarz W. H., and Kleine T. 2012. Thermal evolution and sintering of chondritic planetesimals. *Astronomy & Astrophysics* 537:A45.
- Herzberg C., Raterron P., and Zhang J. 2000. New experimental observations on the anhydrous solidus for peridotite KLB-1. *Geochemistry Geophysics Geosystems* 1:2000GC000089.
- Hevey P. J. and Sanders I. S. 2006. A model for planetesimal meltdown by ^{26}Al and its implications for meteorite parent bodies. *Meteoritics & Planetary Science* 41:95–106.
- Hirschmann M. M. 2000. Mantle solidus: Experimental constraints and the effects of peridotite composition. *Geochemistry Geophysics Geosystems* 1:1042. doi:10.1029/2000GC000070.
- Höink T., Schmalzl J., and Hansen U. 2006. Dynamics of metal-silicate separation in a terrestrial magma ocean. *Geochemistry Geophysics Geosystems* 7:Q09008.
- Jacobsen B., Yin Q.-Z., Moynier F., Amelin Y., Krot A. N., Nagashima K., Hutcheon I. D., and Palme H. 2008. ^{26}Al - ^{26}Mg and ^{207}Pb - ^{206}Pb systematics of Allende CAIs: Canonical solar initial $^{26}\text{Al}/^{27}\text{Al}$ ratio reinstated. *Earth and Planetary Science Letters* 272:353–364.
- Johansen A. and Klahr H. 2011. Planetesimal formation through streaming and gravitational instabilities. *Earth, Moon, and Planets* 108:39–43.
- Johansen A., Oishi J. S., Low M.-M. M., Klahr H., Henning T., and Youdin A. 2007. Rapid planetesimal formation in turbulent circumstellar disks. *Nature* 448:1022–1025.
- Jurewicz A. J. G., Mittlefehldt D. W., and Jones J. H. 1993. Experimental partial melting of the Allende (CV) and Murchison (CM) chondrites and the origin of asteroidal basalts. *Geochimica et Cosmochimica Acta* 57:2123–2139.
- Keil K., Stöffler D., Love S. G., and Scott E. R. D. 1993. Constraints on the role of impact heating and melting in asteroids. *Meteoritics & Planetary Science* 32:349–363.
- Kleine T., Touboul M., Bourdon B., Nimmo F., Mezger K., Palme H., Jacobsen S. B., Yin Q.-Z., and Halliday A. N. 2009. Hf-W chronology of the accretion and early evolution of asteroids and terrestrial planets. *Geochimica et Cosmochimica Acta* 73:5150–5188.
- Kleine T., Hans U., Irving A. J., and Bourdon B. 2012. Chronology of the angrite parent body and implications for core formation in protoplanets. *Geochimica et Cosmochimica Acta* 84:186–203.
- Kraichnan R. H. 1962. Turbulent thermal convection at arbitrary Prandtl number. *The Physics of Fluids* 5:1374–1389.
- Liebske C., Schmickler B., Terasaki H., Poe B. T., Suzuki A., Funakoshi K.-I., Ando R., and Rubie D. C. 2005. Viscosity of peridotite liquid up to 13 GPa: Implications for magma ocean viscosities. *Earth and Planetary Science Letters* 240:589–604.
- Longhi J. 1999. Phase equilibrium constraints on angrite petrogenesis. *Geochimica et Cosmochimica Acta* 63:573–585.
- Mackwell S. J. 1991. High-temperature rheology of enstatite: Implications for creep in the mantle. *Geophysical Research Letters* 18:2027–2030.
- Markowski A., Quitte G., Halliday A. N., and Kleine T. 2006. Tungsten isotopic compositions of iron meteorites: Chronological constraints vs. cosmogenic effects. *Earth and Planetary Science Letters* 242:1–15.
- McCoy T. J., Keil K., Clayton R. N., Mayeda T. K., Bogard D., Garrison D., Huss G. R., Hutcheon I. D., and Wieler R. 1996. A petrologic, chemical, and isotopic study of Monument Draw and comparison with other acapulcoites: Evidence for formation by incipient partial melting. *Geochimica et Cosmochimica Acta* 60:2681–2708.
- McCoy T. J., Keil K., Clayton R. N., Mayeda T. K., Bogard D. D., Garrison D. H., and Wieler R. 1997. A petrologic and isotopic study of lodranites: Evidence for early formation as partial melt residues from heterogeneous precursors. *Geochimica et Cosmochimica Acta* 61:623–637.
- Merk R., Breuer D., and Spohn T. 2002. Numerical modeling of ^{26}Al -induced radioactive melting of asteroids considering accretion. *Icarus* 159:183–191.
- Min M., Dullemond C. P., Kama M., and Dominik C. 2011. The thermal structure and the location of the snow line in the protosolar nebula: Axisymmetric models with full 3-D radiative transfer. *Icarus* 212:416–426.
- Minarik W. G., Ryerson F. J., and Watson E. B. 1996. Textural entrapment of core-forming melts. *Science* 272:530–533.
- Morbidelli A., Bottke W. F., Nesvorný D., and Levison H. F. 2009. Asteroids were born big. *Icarus* 204:558–573.
- Parisi M. G. 2013. Impact disruption of primordial planetesimals. *Planetary and Space Science* 75:96–104.
- Pinkerton H. and Stevenson R. J. 1992. Methods of determining the rheological properties of magmas at subliquidus temperatures. *Journal of Volcanology and Geothermal Research* 53:47–66.
- Qin L., Dauphas N., Wadhwa M., Masarik J., and Janney P. E. 2008. Rapid accretion and differentiation of iron meteorite parent bodies inferred from ^{182}Hf - ^{182}W chronometry and thermal modeling. *Earth and Planetary Science Letters* 273:94–104.

- Ranalli G. 1995. *Rheology of the Earth*, 2nd ed. London: Chapman & Hall. 436 p.
- Righter K. 2008. Siderophile element depletion in the angrite parent body (APB) mantle: Due to core formation? (abstract #1936) 39th Lunar and Planetary Science Conference. CD-ROM.
- Righter K. and Drake M. J. 1996. Core formation in Earth's Moon, Mars, and Vesta. *Icarus* 124:513–529.
- Righter K. and Drake M. J. 1997. A magma ocean on Vesta: Core formation and petrogenesis of eucrites and diogenites. *Meteoritics & Planetary Science* 32:929–944.
- Rubie D., Melosh H. J., Reid J. E., Liebske C., and Righter K. 2003. Mechanisms of metal-silicate equilibration in the terrestrial magma ocean. *Earth and Planetary Science Letters* 205:239–255.
- Rubie D. C., Nimmo F., and Melosh H. J. 2007. Formation of the Earth's core. In *Treatise on geophysics, volume 9: Evolution of the Earth*, edited by Stevenson D. J. Amsterdam: Elsevier B.V. pp. 51–90.
- Rubin A. E. 2007. Petrogenesis of acapulcoites and lodranites: A shock-melting model. *Geochimica et Cosmochimica Acta* 71:2383–2401.
- Ruzicka A., Killgore M., Mittlefehldt D. W., and Fries M. D. 2005. Portales Valley: Petrology of a metallic-melt meteorite breccia. *Meteoritics & Planetary Science* 40:261–295.
- Sahijpal S., Soni P., and Gupta G. 2007. Numerical simulations of the differentiation of accreting planetesimals with ^{26}Al and ^{60}Fe as heat sources. *Meteoritics & Planetary Science* 42:1529–1548.
- Schmelting H., Babeyko A. Y., Enns A., Faccenna C., Funicello F., Gerya T. V., Golabek G. J., Grigull S., Kaus B. J. P., Morra G., Schmalholz S. M., and van Hunen J. 2008. A benchmark comparison of spontaneous subduction models—Towards a free surface. *Physics of the Earth and Planetary Interiors* 171:198–223.
- Schubert G., Spohn T., and Reynolds R. T. 1986. Thermal histories, compositions and internal structures of the moons of the solar system. In *Satellites*, edited by Burns J. A. and Matthews M. S. Tucson, Arizona: The Arizona University Press. pp. 224–292.
- Schwenn M. B. and Goetze C. 1978. Creep of olivine during hot-pressing. *Tectonophysics* 48:41–60.
- Siggia E. D. 1994. High Rayleigh number convection. *Annual Reviews of Fluid Mechanics* 26:137–168.
- Solomatov V. S. 2007. Magma oceans and primordial mantle differentiation. In *Treatise on geophysics, volume 9: Evolution of the Earth*, edited by Stevenson D. J. Amsterdam: Elsevier B.V. pp. 91–119.
- Sotin C. and Labrosse S. 1999. Three-dimensional thermal convection in an iso-viscous, infinite Prandtl number fluid heated from within and from below: Applications to the transfer of heat through planetary mantles. *Physics of the Earth and Planetary Interiors* 112:171–190.
- Stevenson D. J. 1990. Fluid dynamics of core formation. In *Origin of the Earth*, edited by Newsom H. E. and Jones J. H. New York: Oxford University Press. pp. 231–249.
- Stolper E. M. 1975. Petrogenesis of eucrite, howardite and diogenite meteorites. *Nature* 258:220–222.
- Stolper E. M. 1977. Experimental petrology of eucritic meteorites. *Geochimica et Cosmochimica Acta* 41:587–561.
- Stolper E., Walker E., Hager B. H., and Hays J. F. 1981. Melt segregation from partially molten source regions: The importance of melt density and source region size. *Journal of Geophysical Research* 86:6261–6271.
- Suzuki A., Ohtani E., and Kato T. 1998. Density and thermal expansion of a peridotite melt at high pressure. *Physics of the Earth and Planetary Interiors* 107:53–61.
- Tackley P. J., Schubert G., Glatzmaier G. A., Schenk P., and Ratcliff J. T. 2001. Three-dimensional simulations of mantle convection in Io. *Icarus* 149:79–93.
- Tarduno J. A., Cottrell R. D., Nimmo F., Hopkins J., Voronov J., Erickson A., Blackman E., Scott E. R. D., and McKinley R. 2012. Evidence for a dynamo in the main group pallasite parent body. *Science* 338:939–942.
- Thrane K., Bizzarro M., and Baker J. A. 2006. Brief formation interval for refractory inclusions and uniform distribution of ^{26}Al in the early solar system. *The Astrophysical Journal* 646:L159–L162.
- Tkalcec B. J., Golabek G. J., and Brenker F. E. 2013. Solid-state plastic deformation in the dynamic interior of a differentiated asteroid. *Nature Geoscience* 6:93–97.
- Touboul M., Kleine T., and Bourdon B. 2008. Hf-W systematics of cumulate eucrites and the chronology of the eucrite parent body (abstract #2336). 39th Lunar and Planetary Science Conference. CD-ROM.
- Touboul M., Kleine T., Bourdon B., Van Orman J. A., Maden C., and Zipfel J. 2009. Hf-W thermochronometry: II. Accretion and thermal history of the acapulcoite-lodranite parent body. *Earth and Planetary Science Letters* 284:168–178.
- Trønnes R. G. and Frost D. J. 2002. Peridotite melting and mineral melt partitioning of major and minor elements at 22–24.5 GPa. *Earth and Planetary Science Letters* 197:117–131.
- Turcotte D. L. and Schubert G. 2002. *Geodynamics*, 2nd ed. New York: Cambridge University Press. 456 p.
- Usselman T. M. 1975. Experimental approach to state of core: Part 1. Liquidus relations of Fe-rich portion of Fe-Ni-S system from 30 to 100 Kb. *American Journal of Science* 275:278–290.
- Van Orman J. A., Saal A. E., Bourdon B., and Hauri E. H. 2006. Diffusive fractionation of U-series radionuclides during mantle melting and shallow level melt-cumulate interaction. *Geochimica et Cosmochimica Acta* 70:4797–4812.
- Wade J. and Wood B. J. 2005. Core formation and the oxidation state of the Earth. *Earth and Planetary Science Letters* 236:78–95.
- Weiss B. P. and Elkins-Tanton L. 2013. Differentiated planetesimals and the parent bodies of chondrites. *Annual Review of Earth and Planetary Science* 41:529–560.
- Weiss B. P., Berdahl J. S., Elkins-Tanton L., Stanley S., Lima E. A., and Carporzen L. 2008. Magnetism on the angrite parent body and the early differentiation of planetesimals. *Science* 322:713–716.
- Yomogida K. and Matsui T. 1984. Multiple parent bodies of ordinary chondrites. *Earth and Planetary Science Letters* 68:34–42.
- Zahnle K. J., Kasting J. F., and Pollack J. B. 1988. Evolution of a steam atmosphere during Earth's accretion. *Icarus* 74:62–97.
- Zipfel J., Palme H., Kennedy A. K., and Hutcheon I. D. 1995. Chemical composition and origin of the Acapulco meteorite. *Geochimica et Cosmochimica Acta* 59:3607–3627.

SUPPORTING INFORMATION

Additional supporting information may be found in the online version of this article:

Video S1: Evolution of the 3-D thermal structure inside a planetesimal with $R_p = 45$ km and $t_{\text{form}} = 0.73$ Ma after CAI (see also Fig. 3). The bluish contour marks the surface of the planetesimal, while the colored

contours show the 1400 K (yellow), 1500 K (orange), 1600 K (red), and 1630 K (purple) isotherms, respectively.

Video S2: Evolution of the 2-D thermal structure inside a planetesimal with $R_p = 85$ km and $t_{\text{form}} = 1.2775$ Ma after CAI. The white line marks the surface of the planetesimal, while the yellow line corresponds to 19 km depth, a possible formation region of lodranites suggested by 2-D results.
